ARTICLES
https://doi.org/10.1038/s41567-019-0736-9

nature physics

Sixfold enhancement of superconductivity in a tunable electronic nematic system

Chris Eckberg[1*], Daniel J. Campbell[1], Tristin Metz[1], John Collini[1], Halyna Hodovanets[1], Tyler Drye[1], Peter Zavalij[2], Morten H. Christensen[3], Rafael M. Fernandes[3], Sangjun Lee[4], Peter Abbamonte[4], Jeffrey W. Lynn[5] and Johnpierre Paglione[1,6*]

The electronic nematic phase—in which electronic degrees of freedom lower the crystal rotational symmetry—is commonly observed in high-temperature superconductors. However, understanding the role of nematicity and nematic fluctuations in Cooper pairing is often made more complicated by the coexistence of other orders, particularly long-range magnetic order. Here we report the enhancement of superconductivity in a model electronic nematic system that is not magnetic, and show that the enhancement is directly born out of strong nematic fluctuations associated with a quantum phase transition. We present measurements of the resistance as a function of strain in $Ba_{1-x}Sr_xNi_2As_2$ to show that strontium substitution promotes an electronically driven nematic order in this system. In addition, the complete suppression of that order to absolute zero temperature leads to an enhancement of the pairing strength, as evidenced by a sixfold increase in the superconducting transition temperature. The direct relation between enhanced pairing and nematic fluctuations in this model system, as well as the interplay with a unidirectional charge-density-wave order comparable to that found in the cuprates, offers a means to investigate the role of nematicity in strengthening superconductivity.

High-temperature superconductivity in both cuprate[1,2] and iron-based materials[3–5] emerges from a notably complex normal state. Although magnetic spin fluctuations are commonly believed to drive Cooper pairing in both of these families, the common occurrence of a rotational symmetry-breaking nematic phase has captured increasing attention in recent years[6,7]. In contrast to a conventional structural transition, overwhelming evidence suggests that the nematic phase in these compounds is promoted by an electronic instability rather than lattice softening[8,9].

Theoretical analyses have shown that fluctuations associated with such an electronic nematic phase, particularly near a putative quantum critical point, can enhance superconductivity[10–14]. Nematic fluctuations are peaked at zero wavevector, and so favour pairing instabilities in several symmetry channels, in contrast to the case of magnetic fluctuations. Experiments have indeed shown a striking enhancement of nematic fluctuations centred at optimal tuning of superconductivity in a number of iron-based superconductors[8,9], and a strong tendency towards nematicity in high-critical temperature (T_c) cuprate materials[15–17]. However, the overarching presence of magnetic fluctuations emanating from proximate antiferromagnetic instabilities complicates our understanding of the relation between enhanced pairing and nematicity in most nematic materials. The $FeSe_{1-x}S_x$ substitution series is one exception, where the system exhibits both superconductivity and nematicity in the absence of magnetic order[18]. However, in this series, the superconducting transition temperature T_c is virtually unaffected by tuning through the nematic quantum critical point[18,19], leaving open questions about the influence of nematic fluctuations.

Here we present the discovery of electronic nematicity and evidence for nematic-fluctuation-enhanced superconductivity in $Ba_{1-x}Sr_xNi_2As_2$, a seemingly conventional nickel-based superconductor series that is readily tunable by chemical substitution and is void of magnetic order. $BaNi_2As_2$, the nickel-based analogue of the iron-based parent compound $BaFe_2As_2$, is a metallic compound that exhibits a strongly first-order structural transition from tetragonal to triclinic crystal structure at $T_S = 135$ K on cooling. Theoretical consideration has suggested that this structural distortion may originate from a predisposition to orbital ordering[20], and magnetic order has not been found in either the high- or low-temperature phase of $BaNi_2As_2$ to date[21–23]. Additionally, recent X-ray diffraction measurements have provided evidence for a previously unobserved unidirectional and incommensurate charge-density-wave (I-CDW) order that onsets at temperatures slightly above T_S (ref. [24]), followed by an abrupt transition to a new, commensurate CDW (C-CDW) order on cooling into the triclinic phase[24], hinting at a possible relationship between charge order and the structural distortion. In contrast, $SrNi_2As_2$ is tetragonal at all temperatures, and is not reported to exhibit CDW or magnetic order[25]. Both materials superconduct near 0.6 K, and thermodynamic experiments as well as first-principle analysis have indicated that superconductivity is of conventional origin in both materials[26,27]. In this work, we study the superconducting phase and normal state properties of substituted $Ba_{1-x}Sr_xNi_2As_2$ crystals as a function of Ba/Sr content, finding that superconductivity is not only robust but is also dramatically enhanced when electronic nematic fluctuations are maximized at a quantum phase transition.

---

[1] Maryland Quantum Materials Center, Department of Physics, University of Maryland, College Park, MD, USA. [2] Department of Chemistry, University of Maryland, College Park, MD, USA. [3] School of Physics and Astronomy, University of Minnesota, Minneapolis, MN, USA. [4] Department of Physics, Seitz Materials Research Laboratory, University of Illinois at Urbana-Champaign, Urbana, IL, USA. [5] NIST Center for Neutron Research, National Institute of Standards and Technology, Gaithersburg, MD, USA. [6] The Canadian Institute for Advanced Research, Toronto, Ontario, Canada.
*e-mail: eckbergc@umd.edu; paglione@umd.edu

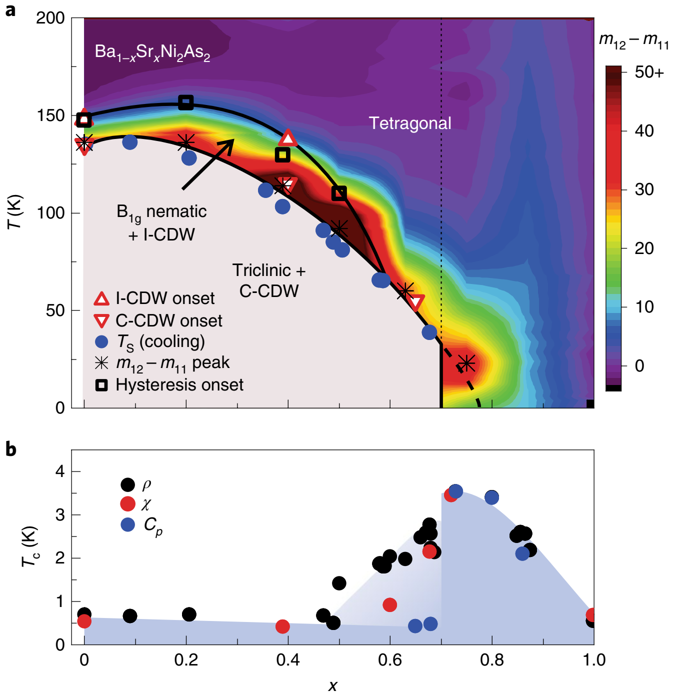

Fig. 1 | Evolution of structural, charge and nematic orders in $Ba_{1-x}Sr_xNi_2As_2$. This system presents an interplay of structural, charge and nematic instabilities that evolve as a function of chemical pressure induced by Sr substitution. It features an enhancement of the superconducting transition temperature in the region where charge and nematic orders cease to be long range, and nematic fluctuations are peaked at the lowest temperatures. **a**, Single-crystal measurements form a phase diagram consisting of onsets of I-CDW order (upright red triangles), elastoresistive strain-hysteresis (open black squares), C-CDW order (inverted red triangles), and the cooling transition of the first-order triclinic structural distortion (filled blue circles). The black asterisks mark the peak position of nematic susceptibilities, which extend beyond the disappearance (vertical dashed line) of the triclinic phase at $x_c = 0.70$. The overlaid colour scale represents interpolated values of the nematic susceptibility $m_{12}-m_{11}$ generated from data taken in $Ba_{1-x}Sr_xNi_2As_2$ single crystals with $x = 0$, 0.2, 0.4, 0.5, 0.63, 0.75, 0.87 and 1.0. **b**, Superconducting transition temperatures T_c in $Ba_{1-x}Sr_xNi_2As_2$ single crystals determined by transport (black circles), magnetization (red circles) and heat capacity (blue circles) measurements. The dark blue shading reflects the true, bulk T_c (as confirmed via heat capacity transitions) while the light blue region indicates filamentary superconductivity observed as broad transitions in transport and magnetic measurements, but absent in heat capacity.

We begin by presenting the global phase diagram of the $Ba_{1-x}Sr_xNi_2As_2$ system in Fig. 1a. Replacing Ba with Sr suppresses the first-order tetragonal–triclinic structural distortion, as well as the simultaneous C-CDW order, in a continuous manner. On increasing x beyond the critical value $x_c = 0.7$, an abrupt 0 K tetragonal–triclinic structural phase transition is observed, and the system remains tetragonal and void of charge order in all samples between x_c and $x = 1$. The I-CDW phase, which appears at temperatures above T_S in pristine $BaNi_2As_2$, is also suppressed with increasing x until it merges with T_S and disappears altogether (upright red triangles in Fig. 1a). Additionally, the coherence length of the I-CDW, estimated from the full-width at half-maximum of its associated X-ray peaks, is reduced from over 1,000 Å to only several hundred ångströms with increasing x between $x = 0$ and $x = 0.4$, and the structure vanishes in samples with larger x. For instance, at $x = 0.65$ the system transitions from a tetragonal structure with no incommensurate charge-order superstructure peaks into a triclinic structure with a C-CDW superstructure at 50 K.

In parallel, superconductivity in $Ba_{1-x}Sr_xNi_2As_2$ single crystals changes across the phase diagram (Fig. 1b). Approaching x_c from the $BaNi_2As_2$ endmember, resistive and magnetic signatures of T_c appear to climb in temperature at concentrations above $x = 0.5$. However, despite the onset of zero resistance at increasing temperature, the 'bulk' signature of T_c, as determined by specific heat measurements (see Supplementary Fig. 6), remains relatively unchanged for $x < x_c$. On crossing the zero-temperature structural phase boundary, an abrupt enhancement in bulk T_c is observed from approximately 0.5 K in $x = 0.68$ samples to near 3.5 K at $x = 0.71$. Optimally substituted $x = 0.71$ presents a very robust superconducting transition as measured by resistivity, diamagnetism and specific heat anomaly, well fitted by a single-band model with a BCS gap (Fig. 2 inset). Remarkably, this optimal T_c of 3.5 K at $x = 0.71$ marks a nearly sixfold enhancement compared to either of the Sr- or Ba-based endmembers. The superconducting transition then decreases continuously with increasing x towards that of $SrNi_2As_2$. This change in pairing strength occurs through a regime with no notable change in structure, and virtually unchanged Sommerfeld coefficients of approximately 10 mJ mol^{-1} K^{-2} (Fig. 2), indicating that the T_c enhancement cannot be explained by changes in the electronic density of states.

Consistent with prior studies[28–30], the $Ba_{1-x}Sr_xNi_2As_2$ system exhibits a discontinuity in the Debye temperature Θ_D at x_c. However, Θ_D remains approximately constant between $x = 0.71$ ($\Theta_D = 198$ K) and $x = 0.86$ ($\Theta_D = 188$ K), despite a nearly twofold difference in the superconducting T_c. This contrast indicates that, like the electronic density of states, changes in lattice stiffness do not capture the enhancement in the pairing potential. Rather, the smooth increase in critical temperature on approaching x_c from above is reminiscent of a fluctuation-driven superconducting enhancement. Given the very abrupt first-order nature of the triclinic–tetragonal structural boundary, which appears to drop at x_c, an increase in pairing strength must arise from a hitherto hidden coupling to the electronic system that can enhance pairing.

Having ruled out the usual sources of a T_c increase expected for a conventional phonon-mediated superconductor (density of states and Debye frequency), we propose that this enhancement is driven by the presence of nematic fluctuations. Indeed, the existence of a tetragonal-to-triclinic transition shows that rotational symmetry is broken in this system. To investigate whether this transition is driven by electronic, rather than lattice degrees of freedom, we perform elastoresistance measurements. The elastoresistance tensor $m_{ij,kl} = \frac{\partial(\Delta\rho/\rho)_{ij}}{\partial\epsilon_{kl}}$ corresponds to the rate of change of the normalized resistivity $(\Delta\rho/\rho)_{ij}$ on application of external strain ϵ_{kl}. As discussed in ref.[8], when the applied strain transforms as one of the non-trivial irreducible representations Γ_μ of the point group, $\epsilon_{kl} \equiv \varepsilon_\mu$, the resistivity change in that channel is proportional to the corresponding nematic order ψ_μ, $(\Delta\rho/\rho)_{ij} \propto \psi_\mu$. As ε_μ acts as a conjugate field to the nematic order parameter ψ_μ, the corresponding elastoresistance m_{Γ_μ} becomes proportional to the bare nematic susceptibility without renormalization by the lattice degrees of freedom:

$$m_{\Gamma_\mu} \propto \chi^{\mu}_{\mathrm{nem}} \equiv \frac{\partial\psi_\mu}{\partial\varepsilon_\mu} \qquad (1)$$

The key point is that, if m_{Γ_μ} shows a diverging behaviour above the rotational symmetry-breaking transition, it implies that the latter is driven by electronic degrees of freedom. If m_{Γ_μ} shows instead a weak temperature dependence, it implies that the transition is a standard lattice-driven structural transition.

In the case of tetragonal $Ba_{1-x}Sr_xNi_2As_2$, there are three symmetry-distinct channels of rotational symmetry-breaking, corresponding to the three irreducible representations B_{1g}, B_{2g} and E_g of

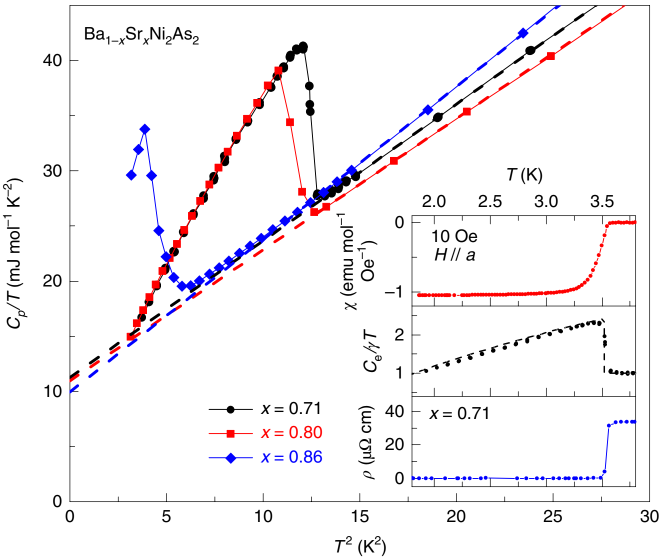

Fig. 2 | Enhancement of superconducting transition temperature. Heat capacity measurements in slightly over-substituted $Ba_{1-x}Sr_xNi_2As_2$ single crystals with $x = 0.71$, 0.80 and 0.86 depict dramatic enhancement of T_c. This contrasts with the very small changes in Sr concentrations, Debye temperatures (as determined by the T^3 phonon contribution shown by the dashed lines) and density of states (as determined by Sommerfeld coefficients, given by the extrapolation of the dashed lines to $T = 0$) across these samples. Inset: the superconducting transition in the same $x = 0.71$ single-crystal specimen, measured by field-cooled magnetization (upper panel), electronic heat capacity (centre panel) and transport (lower panel), is consistent with an enhanced T_c of 3.5 K, larger than the values at either series endmember. The dashed line in the heat capacity data indicates the predicted electronic heat capacity anomaly for a single-band, s-wave superconductor, with a BCS gap[36].

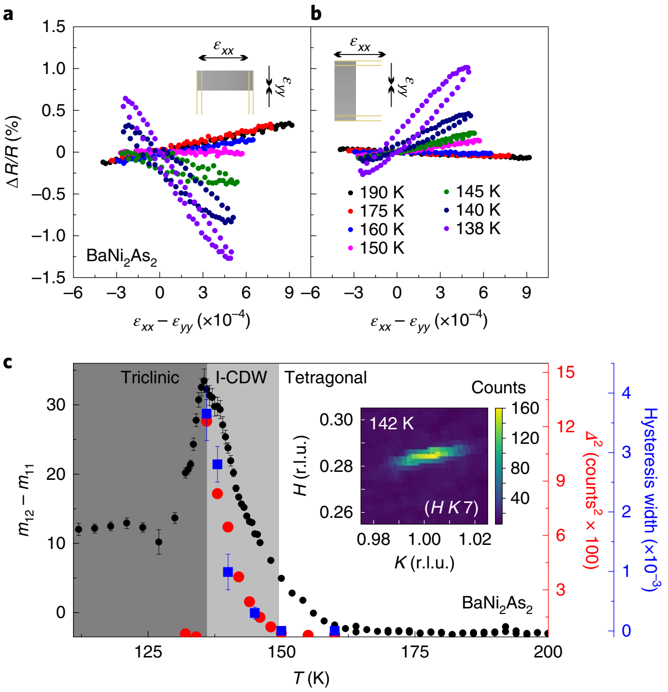

Fig. 3 | Electronic nematic and charge orders in $BaNi_2As_2$. a,b, A divergent B_{1g} nematic susceptibility, determined by elastoresistivity measurements shown in the strain-dependent resistance isotherms for single crystals mounted parallel (**a**) and perpendicular (**b**) to the poling direction of the piezo stack, is comparable in magnitude to that of $BaFe_2As_2$ (ref. [8]) and is accompanied by two notable ordered states. **c**, The nematic susceptibility in the B_{1g} channel, proportional to the elastoresistance $m_{12} - m_{11}$, is nearly flat at high temperatures before growing when approaching the I-CDW-ordered phase (light grey region), and then peaking at the structural transition into the triclinic phase (dark grey region). (Black symbols include error bars representing 90% confidence intervals of data.) Strain-hysteretic behaviour of the elastoresistance is observed to begin at the same temperature where I-CDW is seen. A comparison of the squared peak intensity of a (0.28 0 0) I-CDW superstructure reflection (the (−1.72 1 7) peak; red symbols) and the elastoresistive hysteresis width (blue symbols) shows a nearly linear relationship. Strain-dependent isotherms were repeated three times at each temperature, and hysteresis widths were measured at the widest point. The error bars represent extremal values of the hysteresis width between separate measurements. Inset: an (H K) map (in reciprocal lattice units, r.l.u.) of the reciprocal space at 142 K, displaying a reflection from the superstructure at wavevector (0.28 1 7).

the point group D_{4h}. In terms of charge degrees of freedom, they correspond to quadrupolar charge order with form factors $x^2 - y^2$, xy and (xz, yz), respectively. In terms of lattice degrees of freedom, the first two correspond to orthorhombic distortions $\varepsilon_{B_{1g}}$ and $\varepsilon_{B_{2g}}$, and the third, to a monoclinic distortion $\left(\varepsilon^1_{E_g}, \varepsilon^2_{E_g}\right)$ of the tetragonal lattice. Importantly, in the triclinic phase of $Ba_{1-x}Sr_xNi_2As_2$, all four lattice distortions are present. This indicates the potential that one or more of the three nematic susceptibilities $\chi^{B_{1g}}_{\mathrm{nem}}$, $\chi^{B_{2g}}_{\mathrm{nem}}$ and $\chi^{E_g}_{\mathrm{nem}}$ may be diverging above T_S.

To measure the nematic susceptibilities, we use a piezoelectric elastoresistance technique (see Methods), applying in situ tunable biaxial strain to $Ba_{1-x}Sr_xNi_2As_2$ single-crystal specimens. Figure 3 presents the elastoresistance $m_{12} - m_{11}$, which is proportional to $\chi^{B_{1g}}_{\mathrm{nem}}$, in stoichiometric $BaNi_2As_2$. While $m_{12} - m_{11}$ is negative at temperatures well above the structural transition, it becomes positive near $T_S \approx 135$ K (Fig. 3a,b). Before it peaks at T_S, however, $m_{12} - m_{11}$ starts displaying strain-hysteretic behaviour at a temperature of about 148 K (blue symbols in Fig. 3c). While $m_{12} - m_{11}$ is still presented in the temperature range of strain-hysteretic resistance in Fig. 3c, $T < 148$ K, it is important to note that these values are no longer true nematic susceptibilities, since true nematic susceptibility is well defined only in the regime of linear response. Crucially, the onset of strain-hysteresis in the elastoresistivity experiment coincides with the emergence of I-CDW peaks (red symbols in Fig. 3c), which appear at approximately 150 K. Bragg reflections corresponding to this structure are observed at wavevector (0.28 0 0) while no peaks are observed in the orthogonal (0 0.28 0) direction, indicating that the superstructure does not possess C_4 symmetry. The simultaneous observation of unidirectional CDW peaks and strain-hysteretic $m_{12} - m_{11}$ transport in $BaNi_2As_2$ indicates tetragonal symmetry-breaking in the B_{1g} channel at a temperature $T_N \approx 150$ K that is higher than T_S. However, the electronic nematic susceptibility proportional to $m_{12} - m_{11}$ does not seem to diverge near T_N—in fact, it is nearly temperature-independent above T_N. This is indicative that the transition is driven primarily not by electronic, but by lattice degrees of freedom.

The evolution of the elastoresistivity in the B_{1g} channel in substituted $Ba_{1-x}Sr_xNi_2As_2$ crystals is presented in Fig. 4. First, we note that the onset of strain-hysteretic behaviour at T_N, indicated by the light-grey shaded areas in the plots, moves closer to the triclinic structural transition T_S, and eventually merges with the latter for $x = 0.63$. Second, the modest temperature dependence of $m_{12} - m_{11}$ above T_N in stoichiometric $BaNi_2As_2$ is not reflected in more heavily substituted samples. Indeed, $m_{12} - m_{11}$ starts displaying a diverging behaviour above T_N over a wide temperature range in $Ba_{1-x}Sr_xNi_2As_2$

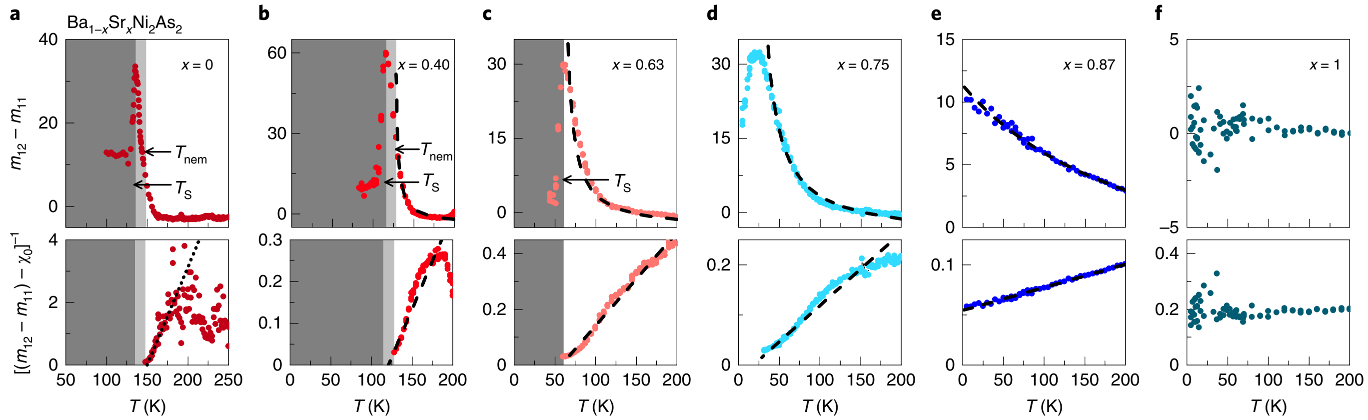

Fig. 4 | Nematic susceptibilities of $Ba_{1-x}Sr_xNi_2As_2$ single crystals. a–f, The B_{1g} nematic susceptibility exhibits a continuous evolution with x, eventually disappearing in $SrNi_2As_2$ ($x=1$), as shown in the top panels. The dark grey regions indicate triclinic structural phases in $x=0$, 0.40 and 0.63, and light grey regions (only in $x=0$ and 0.40) indicate temperatures where elastoresistive hysteresis is observed in the tetragonal structure. The lower panels display the inverse susceptibilities $[(m_{12}-m_{11})-\chi_0]^{-1}$, truncated at the onset of nematic order. The constant, χ_0, is a temperature-independent component of the elastoresistance, coming from factors unrelated to nematic order, including changing sample geometry, and is determined through fitting data to the modified Curie–Weiss functional form; $m_{12}-m_{11}=\frac{\lambda}{a_0(T-T_{N0})}+\chi_0$. The bare nematic transition temperature T_{N0} extracted from such a fit may differ slightly from the observed nematic transition temperature due to coupling between the structural and electronic degrees of freedom. The black dashed lines show the results of this fitting. No fitting is presented in samples of $x=0$ or $x=1$, as neither of these show Curie–Weiss-like divergence. The dotted black line in the lower panel of **a** is a guide for the eye, indicating incipient nematic fluctuations in the vicinity of T_N. At $x=0.75$, which exhibits no nematic, structural or charge-ordered transitions and remains tetragonal to the lowest temperatures, the nematic susceptibility exhibits a broad peak at 25 K.

samples with increasing x. These data may be reasonably fitted to a modified Curie–Weiss function ($\chi_{\mathrm{nem}}^{B_{1g}}=\frac{\lambda}{a_0(T-T_N)}+\chi_0$) above T_N, indicating diverging susceptibilities reminiscent of electronically driven nematic order. Therefore, our elastoresistance data show a change in the character of the tetragonal symmetry-breaking transition from lattice-driven for small x to electronically driven for x near optimal substitution. This is corroborated by a phenomenological Ginzburg–Landau calculation to model the nematic susceptibility data (see Supplementary Section I).

While the B_{1g} nematic susceptibility diverges, the B_{2g} susceptibility is only very weakly temperature dependent in samples with $x=0$ and $x=0.63$ (see Supplementary Figs. 10 and 11). The absence of a diverging B_{2g} susceptibility indicates that the strengthening of the electronic nematic fluctuations is limited to the B_{1g} symmetry channel, despite the presence of B_{2g} symmetric rotational symmetry-breaking at the triclinic structural transition. This indicates that the triclinic phase transition cannot be attributed solely to electronic degrees of freedom, and contrasts with the structurally related Fe-based superconductors, where ubiquitous signatures of nematicity in the B_{2g} channel are reported[9].

The diverging B_{1g} susceptibility persists in the $x=0.75$ samples, which feature no discernible phase transition in thermal, magnetic, transport or diffraction measurements down to the lowest temperatures. Despite the absence of any evident phase transition, $m_{12}-m_{11}$ data for $Ba_{0.25}Sr_{0.75}Ni_2As_2$ exhibit a clear peak and subsequent downturn at 25 K. Such a nematic susceptibility peak, in the absence of any apparent order (see Supplementary Fig. 12), is unprecedented in its observation. In analogy to more familiar magnetic systems, it may be an indication of a freezing nematic glass, or possibly an artefact of quenched disorder subverting long-range nematic correlations.

Returning to the overall phase diagram of $Ba_{1-x}Sr_xNi_2As_2$, the amplitude of the B_{1g} nematic susceptibility is overlaid with the triclinic and CDW phase boundaries in Fig. 1. Owing to our inability to extract a nematic susceptibility in the triclinic phase, as well as the uncertainty in the superconducting T_c in undersubstituted samples, we focus our analysis on crystals that are tetragonal to lowest temperatures. Approaching x_c from the $SrNi_2As_2$ endmember, a smooth enhancement of electronic nematic fluctuations is observed at the lowest temperatures. In contrast to the stagnant behaviour of other thermodynamic quantities, such as specific heat, nematic fluctuations grow concurrently with the enhancing superconducting T_c, with an over tenfold enhancement of $m_{12}-m_{11}$ from $x=1$ to x_c. It is through the exchange of these excitations that the superconducting enhancement in the tetragonal phase can be explained[11,13,14]. The strength of this enhancement, corresponding to a nearly sixfold increase in T_c from the series endmembers, establishes nematic fluctuations as a promising mechanism for enhancing Cooper pairing, even in a conventional superconductor such as, presumably, the one studied here.

The origin of the nematic order in $Ba_{1-x}Sr_xN_2As_2$ cannot be inferred solely from elastoresistance measurements. In the structurally and chemically similar $BaFe_2As_2$ compounds, the B_{2g} electronic nematic order is proposed to be driven by magnetic degrees of freedom, since the stripe magnetic ground state breaks the tetragonal symmetry in the same channel[31–33]. The $Ba_{1-x}Sr_xNi_2As_2$ series, in contrast, exhibits B_{1g} symmetric nematic fluctuations and no known magnetic order. It does exhibit, however, unidirectional CDW order that breaks tetragonal symmetry in the B_{1g} channel. It is therefore tempting to attribute the nematic instability in $Ba_{1-x}Sr_xNi_2As_2$ as driven by charge fluctuations. Indeed, comparing in Fig. 3c the square of the CDW X-ray peak intensity to the width of the elastoresistance hysteresis, which is a proxy of the nematic order parameter (see Supplementary Section I), we observe a nearly linear relationship between the two quantities, as expected by symmetry considerations. This lends further support to the assumption of charge-driven nematicity, although, as the origins of and relationship between I-CDW and C-CDW phases has not been determined yet, it is impossible to conclude if one of the two present charge orders is predominantly associated with the underlying nematicity. Ultimately, these observations provide a compelling scenario to explain the phase diagram of $Ba_{1-x}Sr_xNi_2As_2$ in terms of two cooperative ordered states: a charge-driven electronic nematic phase and a lattice-driven triclinic phase. While both break the tetragonal symmetry in the B_{1g} channel, the latter also breaks additional symmetries that our elastoresistance measurements show cannot be accounted for solely by electronic degrees of freedom (as evidenced by the lack of divergence of the B_{2g} nematic susceptibility).

The likely relationship between nematic and CDW order evokes comparison to the cuprate superconductors, where short-range, unidirectional I-CDW stripe order and electronic anisotropies were reported in the pseudogap phase[7,16,34]. In the cuprates, it was proposed that the microscopic tendency is towards unidirectional CDW order, with long-range coherence being precluded by quenched disorder[35]. The nematic phase is more robust to disorder, however, surviving as a vestige of the suppressed stripes. In $Ba_{1-x}Sr_xNi_2As_2$, unlike the cuprate compounds, long-range CDW superstructures survive for sufficiently small x.

Online content

Any methods, additional references, Nature Research reporting summaries, source data, extended data, supplementary information, acknowledgements, peer review information; details of author contributions and competing interests; and statements of data and code availability are available at https://doi.org/10.1038/s41567-019-0736-9.

Received: 2 April 2019; Accepted: 5 November 2019;
Published online: 23 December 2019

References

1. Orenstein, J. & Millis, A. J. Advances in the physics of high-temperature superconductivity. *Science* **288**, 468–474 (2000).
2. Keimer, B., Kivelson, S. A., Norman, M. R., Uchida, S. & Zaanen, J. From quantum matter to high-temperature superconductivity in copper oxides. *Nature* **518**, 179–186 (2015).
3. Paglione, J. & Greene, R. High-temperature superconductivity in iron-based materials. *Nat. Phys.* **6**, 645–658 (2010).
4. Johnston, D. C. The puzzle of high temperature superconductivity in layered iron pnictides and chalcogenides. *Adv. Phys.* **59**, 803–1061 (2010).
5. Stewart, G. R. Superconductivity in iron compounds. *Rev. Mod. Phys.* **83**, 1589–1652 (2011).
6. Fernandes, R. M., Chubukov, A. V. & Schmalian, J. What drives nematic order in iron-based superconductors? *Nat. Phys.* **10**, 97–104 (2014).
7. Kivelson, S., Fradkin, E. & Emery, V. Electronic liquid crystal phases of a doped Mott insulator. *Nature* **393**, 550–553 (1998).
8. Chu, J.-H., Kuo, H.-H., Analytis, J. G. & Fisher, I. R. Divergent nematic susceptibility in an iron arsenide superconductor. *Science* **337**, 710–712 (2012).
9. Kuo, H.-H., Chu, J.-H., Palmstrom, J. C., Kivelson, S. A. & Fisher, I. R. Ubiquitous signatures of nematic quantum criticality in optimally doped Fe-based superconductors. *Science* **352**, 958–962 (2016).
10. Metlitski, M. A., Mross, D. F., Sachdev, S. & Senthil, T. Cooper pairing in non-Fermi liquids. *Phys. Rev. B* **91**, 115111 (2015).
11. Lederer, S., Schattner, Y., Berg, E. & Kivelson, S. A. Enhancement of superconductivity near a nematic quantum critical point. *Phys. Rev. Lett.* **114**, 097001 (2015).
12. Lederer, S., Schattner, Y., Berg, E. & Kivelson, S. A. Superconductivity and non-Fermi liquid behavior near a nematic quantum critical point. *Proc. Natl Acad. Sci. USA* **114**, 4905–4910 (2017).
13. Kang, J. & Fernandes, R. M. Superconductivity in FeSe thin films driven by the interplay between nematic fluctuations and spin–orbit coupling. *Phys. Rev. Lett.* **117**, 217003 (2016).
14. Klein, A., Wu, Y. & Chubukov, A.V. Multiple intertwined pairing states and temperature-sensitive gap anisotropy for superconductivity at a nematic quantum-critical point. *npj Quantum Mater.* **4**, 55 (2019).
15. Hinkov, V. et al. Electronic liquid crystal state in the high-temperature superconductor $YBa_2Cu_2O_2$. *Science* **319**, 597–600 (2008).
16. Vojta, M. Lattice symmetry breaking in cuprate superconductors: stripes, nematics, and superconductivity. *Adv. Phys.* **58**, 699–820 (2009).
17. Sato, Y. et al. Thermodynamic evidence for a nematic phase transition at the onset of the pseudogap in $YBa_2Cu_2O_2$. *Nat. Phys.* **13**, 1074–1078 (2017).
18. Hosoi, S. et al. Nematic quantum critical point without magnetism in $FeSe_{1-x}S_{1-x}$ superconductor. *Proc. Natl Acad. Sci. USA* **113**, 8139–8143 (2016).
19. Reiss, P. et al. Suppression of electronic correlations by chemical pressure from FeSe to FeS. *Phys. Rev. B* **96**, 121103 (2017).
20. Yamakawa, Y., Onari, S. & Kontani, H. Zigzag chain structure transition and orbital fluctuations in Ni-based superconductors. *J. Phys. Soc. Jpn* **82**, 094704 (2013).
21. Ronning, F. et al. The first order phase transition and superconductivity in $BaNi_2As_2$ single crystals. *J. Phys. Condens. Matter* **20**, 342203 (2008).
22. Sefat, A. S. et al. Structure and anisotropic properties of $BaFe_{2-x}Ni_{2-x}As_{2-x}$ ($x=0$, 1, and 2) single crystals. *Phys. Rev. B* **79**, 094508 (2009).
23. Kothapalli, K., Ronning, F., Bauer, E. D., Schultz, A. J. & Nakotte, H. Single-crystal neutron diffraction studies on Ni-based metal-pnictide superconductor $BaNi_2As_2$. *J. Phys. Conf. Ser.* **251**, 012010 (2010).
24. Lee, S. et al. Unconventional charge density wave order in the pnictide superconductor $Ba(Ni_{1-x}Co_{1-x})_{1-x}As_{1-x}$. *Phys. Rev. Lett.* **122**, 147601 (2019).
25. Bauer, E. D., Ronning, F., Scott, B. L. & Thompson, J. D. Superconductivity in $SrNi_2As_2$ single crystals. *Phys. Rev. B* **78**, 172504 (2008).
26. Subedi, A. & Singh, D. J. Density functional study of $BaNi_2As_2$: electronic structure, phonons, and electron–phonon superconductivity. *Phys. Rev. B* **78**, 132511 (2008).
27. Kurita, N. et al. Low-temperature magnetothermal transport investigation of a Ni-based superconductor $BaNi_2As_2$: evidence for fully gapped superconductivity. *Phys. Rev. Lett.* **102**, 147004 (2009).
28. Kudo, K., Takasuga, M., Okamoto, Y., Hiroi, Z. & Nohara, M. Giant phonon softening and enhancement of superconductivity by phosphorus doping of $BaNi_2As_2$. *Phys. Rev. Lett.* **109**, 097002 (2012).
29. Kudo, K., Takasuga, M. & Nohara, M. Copper doping of $BaNi_2As_2$: giant phonon softening and superconductivity enhancement. Preprint at http://arXiv.org/abs/1704.04854 (2017).
30. Eckberg, C. et al. Evolution of structure and superconductivity in $Ba(Ni_{1-x}Co_{1-x})_{1-x}As_{1-x}$. *Phys. Rev. B* **97**, 224505 (2018).
31. Cano, A., Civelli, M., Eremin, I. & Paul, I. Interplay of magnetic and structural transitions in iron-based pnictide superconductors. *Phys. Rev. B* **82**, 020408 (2010).
32. Fernandes, R. M., Chubukov, A. V., Knolle, J., Eremin, I. & Schmalian, J. Preemptive nematic order, pseudogap, and orbital order in the iron pnictides. *Phys. Rev. B* **85**, 024534 (2012).
33. Fernandes, R. M., Böhmer, A. E., Meingast, C. & Schmalian, J. Scaling between magnetic and lattice fluctuations in iron pnictide superconductors. *Phys. Rev. Lett.* **111**, 137001 (2013).
34. Achkar, A. J. et al. Nematicity in stripe-ordered cuprates probed via resonant x-ray scattering. *Science* **351**, 576–578 (2016).
35. Nie, L., Tarjus, G. & Kivelson, S. A. Quenched disorder and vestigial nematicity in the pseudogap regime of the cuprates. *Proc. Natl Acad. Sci. USA* **111**, 7980–7985 (2014).
36. Johnston, D. C. Elaboration of the α-model derived from the BCS theory of superconductivity. *Supercond. Sci. Technol.* **26**, 115011 (2013).

Methods

Crystal synthesis. $Ba_{1-x}Sr_xNi_2As_2$ single crystals were synthesized using pre-reacted NiAs self-flux combined with Ba and Sr pieces in a 4:1−x:x ratio as previously reported[22]. Materials were heated to 1,180 °C before being slowly cooled to 980 °C at 2 °C h^{-1}. At this point, the furnace was turned off and allowed to cool to room temperature naturally. Once cool, crystals with typical dimensions of 2 mm × 2 mm × 0.5 mm were mechanically extracted from flux. The chemical compositions of the resulting crystals were determined using a combination of energy-dispersive spectroscopy and single-crystal X-ray refinements.

Transport, specific heat and magnetization. Transport and heat capacity data were taken using both a Quantum Design Physical Property Measurement System and a Quantum Design DynaCool. Heat capacity data were generally collected via a relaxation method. To observe the first-order phase transition on both warming and cooling, select heat capacity measurements were modified to be sensitive to both transitions. Within these modified measurements, an extended heat pulse was applied and heat capacity was extracted using a local derivative approach. D.c.-magnetization measurements were taken using a SQUID-VSM option in a Quantum Design MPMS3 system. A home-made coil[37] was also used in a Quantum Design adiabatic demagnetization refrigerator insert to measure a.c. susceptibility down to 0.1 K.

X-ray diffraction. The 250 K structural data were collected on single crystals in a Bruker APEX-II CCD system equipped with a graphite monochromator and a MoKα sealed tube ($\lambda = 0.71073$ Å), and were refined using the Bruker SHELXTL Software Package. Temperature-dependent diffraction measurements were carried out using a Xenocs GeniX 3D MoKα microspot X-ray source with multilayer focusing optics and a Mar345 image plate detector. Single-crystal samples were cooled with a closed-cycle cyrostat and mounted to a Huber four-circle diffractometer.

Elastoresistivity. To measure the nematic susceptibilities, we used the piezoelectric elastoresistance technique of refs. [8,38]. Within the D_{4h} point group, elastoresistive coefficients $m_{12} - m_{11}$ are directly proportional to $\chi_{\mathrm{nem}}^{\mathrm{B_{1g}}}$ while m_{66} is directly proportional to $\chi_{\mathrm{nem}}^{\mathrm{B_{2g}}}$ (ref. [39]). Both $m_{12} - m_{11}$ and m_{66} were measured in samples adhered directly to a lead zirconium titanate piezoelectric stack using a strain-transmitting epoxy as discussed in refs. [8,38]. By applying a voltage to the stack, variable bi-axial strain was applied in situ. The magnitude of the applied strain was measured using a strain gauge mounted on the reverse side of the stack. The strain was measured along a single piezo axis (ε_{xx} in the convention used within this text), and orthogonal strain was calculated using the known Poisson's ratio of the stack. $m_{12} - m_{11}$ elastoresistive coefficients were measured using two samples mounted in a mutual orthogonal geometry, with the crystal (1 0 0) axis mounted parallel and perpendicular to the piezo poling direction. For all measurements requiring two samples, a single crystal was polished to a suitable thickness (≤60 μm) and then cleaved into two pieces. These two pieces were used for a single measurement to ensure consistent physical properties across the two orthogonal samples. m_{66} data were collected using a single sample wired in a transverse geometry. Strain was then applied along the crystallographic (1 1 0) direction[38]. Crystal geometry (specifically a narrow c-axis cross-section and tendency towards cleaving along the crystallographic (1 0 0) direction) made m_{44}, $\chi_{\mathrm{nem}}^{\mathrm{E_g}}$, experimentally inaccessible.

Data availability

Source data for Figs. 1–4 are provided with the paper. All other data that support the plots within this paper and other findings of this study are available from the corresponding author upon reasonable request.

References

37. Yonezawa, S., Higuchi, T., Sugimoto, Y., Sow, C. & Maeno, Y. Compact AC susceptometer for fast sample characterization down to 0.1 K. *Rev. Sci. Instrum.* **86**, 093903 (2015).
38. Shapiro, M. C., Hristov, A. T., Palmstrom, J. C., Chu, J.-H. & Fisher, I. R. Measurement of the B_{1g} and B_{2g} components of the elastoresistivity tensor for tetragonal materials via transverse resistivity configurations. *Rev. Sci. Instrum.* **87**, 063902 (2016).
39. Shapiro, M. C., Hlobil, P., Hristov, A. T., Maharaj, A. V. & Fisher, I. R. Symmetry constraints on the elastoresistivity tensor. *Phys. Rev. B* **92**, 235147 (2015).

Acknowledgements

Research at the University of Maryland was supported by the AFOSR Grant No. FA9550-14-10332, the National Science Foundation Grant No. DMR1905891, and the Gordon and Betty Moore Foundation's EPiQS Initiative through Grant No. GBMF4419. We also acknowledge support from the Maryland Quantum Materials Center as well as the Maryland Nanocenter and its FabLab. The identification of any commercial product or trade name does not imply endorsement or recommendation by the National Institute of Standards and Technology. Theory work (R.M.F. and M.H.C.) was supported by the US Department of Energy, Office of Science, Basic Energy Sciences under award number DE-SC0012336. X-ray experiments at UIUC were supported by DOE grant DE-FG02-06ER46285. P.A. acknowledges support from the Gordon and Betty Moore Foundation's EPiQS initiative through grant GBMF4542.

Author contributions

C.E. and J.P. conceived and designed the experiments. C.E., D.J.C., T.M., H.H. and T.D. synthesized crystals and performed basic physical characterization. C.E. performed elastoresistivity measurements. J.C., S.L. and P.A. performed and analysed low-temperature X-ray characterization of the CDW phase. P.Z. performed and analysed 250 K single-crystal X-ray diffraction. J.L. performed preliminary neutron diffraction studies. M.H.C. and R.M.F. developed the phenomenological model describing the evolution of nematicity in this system. C.E., J.P., R.M.F. and M.H.C. wrote the manuscript with contributions from all authors.

Competing interests

The authors declare no competing interests.

Additional information

Supplementary information is available for this paper at https://doi.org/10.1038/s41567-019-0736-9.

Correspondence and requests for materials should be addressed to C.E. or J.P.

Peer review information *Nature Physics* thanks Dimitri Basov and the other, anonymous, reviewer(s) for their contribution to the peer review of this work.

Reprints and permissions information is available at www.nature.com/reprints.

nature physics

SUPPLEMENTARY INFORMATION

https://doi.org/10.1038/s41567-019-0736-9

Sixfold enhancement of superconductivity in a tunable electronic nematic system

Chris Eckberg[1]*, Daniel J. Campbell[1], Tristin Metz[1], John Collini[1], Halyna Hodovanets[1], Tyler Drye[1], Peter Zavalij[2], Morten H. Christensen[3], Rafael M. Fernandes[3], Sangjun Lee[4], Peter Abbamonte[4], Jeffrey W. Lynn[5] and Johnpierre Paglione[1,6]*

[1]Maryland Quantum Materials Center, Department of Physics, University of Maryland, College Park, MD, USA. [2]Department of Chemistry, University of Maryland, College Park, MD, USA. [3]School of Physics and Astronomy, University of Minnesota, Minneapolis, MN, USA. [4]Department of Physics, Seitz Materials Research Laboratory, University of Illinois at Urbana-Champaign, Urbana, IL, USA. [5]NIST Center for Neutron Research, National Institute of Standards and Technology, Gaithersburg, MD, USA. [6]The Canadian Institute for Advanced Research, Toronto, Ontario, Canada.
*e-mail: eckbergc@umd.edu; paglione@umd.edu

Supplemental Information: Sixfold enhancement of superconductivity in a tunable electronic nematic system

I. PHENOMENOLOGICAL MODEL

To model the nematic and triclinic phase transitions in $\mathrm{Ba}_{1-x}\mathrm{Sr}_x\mathrm{Ni}_2\mathrm{As}_2$, we use a phenomenological Landau free-energy expansion. We first focus on the elastic contribution to the free energy. Since $\mathrm{BaNi}_2\mathrm{As}_2$ has a tetragonal crystal structure at high temperatures, the harmonic part of the elastic free energy is written, in the compactified Voigt notation, as [1]

$$\mathcal{F}_{\mathrm{elast}} = \sum_{ij}^{6} \varepsilon_i C_{ij} \varepsilon_j \, , \tag{S1}$$

Here, the strain fields ε_i are

$$\varepsilon_1 = \partial_x u_x + \partial_y u_y + \partial_z u_z \, , \tag{S2}$$

$$\varepsilon_2 = \frac{1}{6}\left(\partial_x u_x + \partial_y u_y - 2\partial_z u_z\right) \, , \tag{S3}$$

$$\varepsilon_3 = \frac{1}{\sqrt{2}}\left(\partial_x u_x - \partial_y u_y\right) \, , \tag{S4}$$

$$\varepsilon_4 = \frac{1}{2}\left(\partial_y u_z + \partial_z u_y\right) \, , \tag{S5}$$

$$\varepsilon_5 = \frac{1}{2}\left(\partial_x u_z + \partial_z u_x\right) \, , \tag{S6}$$

$$\varepsilon_6 = \frac{1}{2}\left(\partial_x u_y + \partial_y u_x\right) \, , \tag{S7}$$

where u_i are the components of the displacement vector and C_{ij} is a matrix containing the elastic moduli. Here we shall focus on the modes that lead to some form of rotational symmetry breaking, which correspond to ε_3, ε_4, ε_5, and ε_6. ε_1 and ε_2 correspond to structural deformations that do not break the tetragonal symmetry. In the language of irreducible representations (irreps) of the tetragonal group, ε_3 transforms as B_{1g}, ε_6 as B_{2g} and ε_4 and ε_5 constitute the two components of an E_g irrep. The condensation of either ϵ_3 or ϵ_6 leads to orthorhombic crystal structures, while ε_4 and/or ε_5 result in a monoclinic structure. On the other hand, a triclinic structure only occurs if all four order parameters, ε_3, ε_4, ε_5, and ε_6, are non-zero.

Focusing on these terms and going beyond the harmonic approximation, the elastic free energy becomes:

$$\begin{aligned}\mathcal{F}_{\mathrm{elast}} = {} & \frac{1}{2}\left(C_{11}-C_{12}\right)\varepsilon_3^2 + \frac{1}{2}C_{66}\varepsilon_6^2 + \frac{1}{2}C_{44}\left(\varepsilon_4^2+\varepsilon_5^2\right) + \lambda_2\varepsilon_4\varepsilon_5\varepsilon_6 + \lambda_3\left(\varepsilon_4^2-\varepsilon_5^2\right)\varepsilon_3 + \\ & \frac{u_1}{4}\varepsilon_3^4 + \frac{u_2}{4}\varepsilon_6^4 + \frac{u_3}{4}\left(\varepsilon_4^2+\varepsilon_5^2\right)^2 - \frac{g_3}{4}\left(\varepsilon_4^2-\varepsilon_5^2\right)^2 \, ,\end{aligned} \tag{S8}$$

where we have neglected quartic terms that will not be important for the analysis below. Note that the cubic terms imply that the condensation of ε_4 and/or ε_5 necessarily leads to a non-zero ε_3 and/or ε_6, since $\varepsilon_6 \sim \varepsilon_4\varepsilon_5$ and $\varepsilon_3 \sim \varepsilon_4^2 - \varepsilon_5^2$. Among the quartic terms, $g_3 > 0$ favors condensation of either ε_4 or ε_5, whereas $g_3 < 0$ favors the simultaneous condensation of both ε_4 and ε_5. Because in the triclinic phase $\varepsilon_3, \varepsilon_4, \varepsilon_5, \varepsilon_6 \neq 0$, a direct tetragonal-to-triclinic transition can only be first-order. As explained in the main text, our data on undoped and underdoped $\mathrm{Ba}_{1-x}\mathrm{Sr}_x\mathrm{Ni}_2\mathrm{As}_2$ suggests symmetry breaking in the B_{1g} channel (i.e. $\varepsilon_3 \neq 0$) before the onset of a triclinic phase. Thus, the transition from tetragonal to triclinic seems to happen via an intermediate orthorhombic phase, at least for sufficiently underdoped compositions.

To understand this sequence of transitions, consider the condensation of a finite $\langle\varepsilon_3\rangle \neq 0$ (either due to the softening of the $C_{11} - C_{12}$ elastic constant or as a consequence of an electronic nematic transition) and integrate out the ε_6 degrees of freedom. The elastic free energy becomes:

$$\mathcal{F}_{\mathrm{elast}} = \frac{1}{2}\left(C_{44}+\lambda_3\langle\varepsilon_3\rangle\right)\varepsilon_4^2 + \frac{1}{2}\left(C_{44}-\lambda_3\langle\varepsilon_3\rangle\right)\varepsilon_5^2 + \frac{\left(u_3 - \frac{\lambda_2^2}{2C_{66}}\right)}{4}\left(\varepsilon_4^2+\varepsilon_5^2\right)^2 - \frac{\left(g_3 - \frac{\lambda_2^2}{2C_{66}}\right)}{4}\left(\varepsilon_4^2-\varepsilon_5^2\right)^2 .$$

A triclinic phase transition can then take place when both C_{44} and C_{66} are soft enough. Indeed, when the elastic constant C_{44} is small enough such that $C_{44} < \lambda_3|\langle\varepsilon_3\rangle|$, either ϵ_4 or ϵ_5 will condense depending on the signs of $\langle\varepsilon_3\rangle$

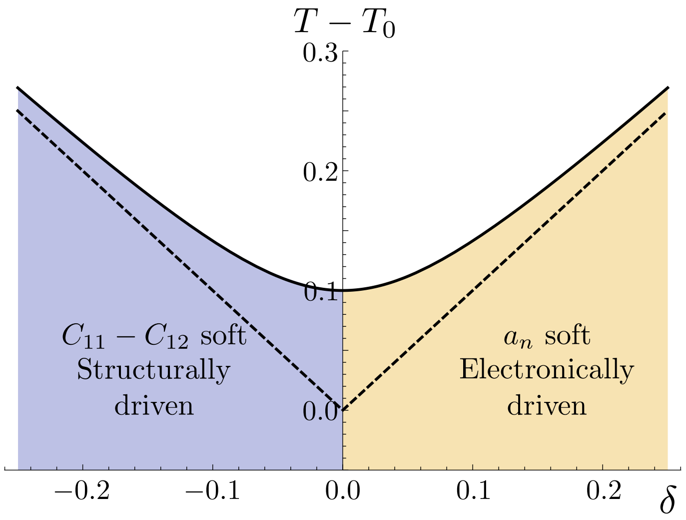

FIG. S1. **Phase diagram for the coupled structural-nematic transition.** The transition temperature $T_{\mathcal{N}}$ (full line) is affected by the finite coupling, λ_1, between the structural and electronic degrees of freedom. Here we set $\lambda_1 = 0.10$. In the absence of λ_1, the transition temperature is given by the dashed line.

and λ_3. When C_{66} is also soft enough, such that $C_{66} < \lambda_2^2/2g_3$, or if g_3 is itself negative, the quartic term favors the simultaneous appearance of both ε_4 and ε_5, which in turn generates ε_6. This is one possible scenario for the transition from tetragonal to triclinic. Whether it occurs via an intermediate orthorhombic (i.e. $\langle\varepsilon_3\rangle \neq 0$) phase taking place at a temperature $T_{\mathcal{N}}$ above the onset of the triclinic order at T_S depends on the character of the orthorhombic transition itself. If the latter is second order, one certainly expects the intermediate phase to appear. However, if the transition is first-order, it can trigger a triclinic phase immediately, resulting in a first-order tetragonal-to-triclinic transition. The latter seems to be the case for compositions closer to the overdoped regime.

The remaining question left in this scenario is whether ε_3 condenses as the result of a lattice instability or as an indirect consequence of the onset of the electronic nematic order parameter ψ that transforms as the B_{1g} irrep. The observation of CDW peaks at the (incommensurate) ordering vector $\mathbf{Q}_1 = (q\ 0\ 0)$ suggest a possible charge-driven electronic nematic phase. Indeed, denoting by Δ_1 the CDW order parameter with ordering vector $\mathbf{Q}_1$ and by Δ_2 the CDW with ordering vector $\mathbf{Q}_2 = (0\ q\ 0)$, CDW fluctuations can lead to a nematic order parameter $\psi \propto \Delta_1^2 - \Delta_2^2$. For our phenomenological analysis, however, the microscopic origin of the nematic order parameter ψ is not important. The free energy expansion including the electronic nematic degrees of freedom is given by:

$$\mathcal{F}_{\mathrm{elast-nem}} = \frac{a_s}{2}\varepsilon_3^2 + \frac{u_s}{4}\varepsilon_3^4 + \frac{a_n}{2}\psi^2 + \frac{u_n}{4}\psi^4 - \lambda_1\psi\varepsilon_3\,. \tag{S9}$$

The last term is the symmetry allowed bilinear coupling between the nematic order parameter and the orthorhombic distortion. Here, the coefficient $a_s = C_{11} - C_{12}$, whereas the coefficient a_n is proportional to the inverse of the bare nematic susceptibility, χ_{nem}^{-1}. As usual, we write $a_n = c_n\,(T - T_{n,0})$ and $a_s = c_s(T - T_{s,0})$, with $T_{n,0}$ the bare nematic transition temperature and $T_{s,0}$, the bare structural transition temperature. Hereafter, we set $c_s = c_n = 1$ for simplicity.

A state with non-zero ε_3 and ψ can be the result of a vanishing a_s (lattice-driven) or of a vanishing a_n (electronic-driven). To model the crossover from a lattice-driven transition ($T_{s,0} < T_{n,0}$) to an electronic-driven transition ($T_{n,0} < T_{s,0}$), we define $T_{n,0} \equiv T_0\,(1+\delta)$ and $T_{s,0} \equiv T_0\,(1-\delta)$. Of course, T_0 and δ in principle depend on the doping composition x. For our purposes, however, which is to contrast the behavior of the elastoresistance in the lattice-driven and electronic-driven regimes, we consider them independent variables and fix T_0 while varying δ.

The resulting (δ, T) phase diagram is shown in Fig. S1. Obviously, there is a single transition at $T_{\mathcal{N}}$ to a state that lowers the tetragonal symmetry of the system down to orthorhombic, given by the solid line. In the limit $\delta \ll -1$, the transition temperature approaches $T_{s,0}$, whereas in the limit $\delta \gg 1$, the transition approaches $T_{n,0}$.

Our goal is to compute the quantity $\frac{\partial\psi}{\partial\varepsilon_3}$, which is proportional to the elastoresistance $m_{12} - m_{11}$ in the disordered state, for different values of δ. A straightforward calculation gives:

$$\frac{\partial\psi}{\partial\varepsilon_3} = \frac{\lambda_1}{a_n + 3u_n\phi^2}\,. \tag{S10}$$

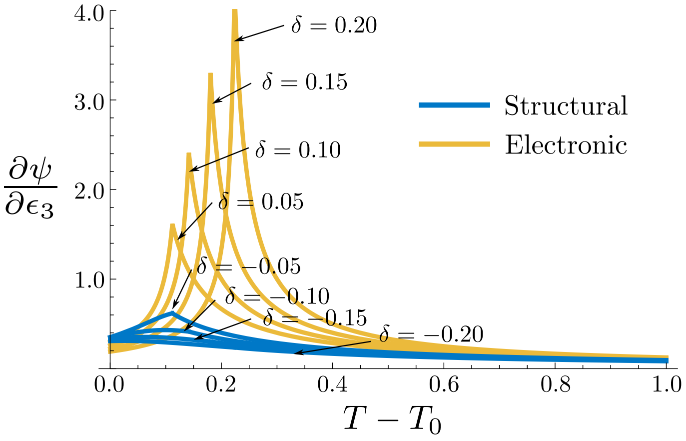

FIG. S2. **Nematic susceptibility in both structurally-driven ($\delta < 0$) and electronically-driven ($\delta > 0$) regimes**. Here δ ranges from $\delta = -0.20$ to $\delta = 0.20$. A sharp peak is evident in the electronically driven case. The parameters used were $\lambda_1 = 0.1$, $u_n = 1.0$, and $u_s = 1.0$.

In Fig. S2, we plot $\frac{\partial\psi}{\partial\varepsilon_3}$ as a function of T for different values of δ, corresponding to both the structurally driven ($\delta < 0$) and electronically ($\delta > 0$) driven cases. In the structurally driven regime, there is no obvious sign of a transition in $\frac{\partial\psi}{\partial\varepsilon_3}$ at $T_{\mathcal{N}}$, as this quantity remains nearly temperature-independent or displays a mild peak. This is a consequence of the fact that the bare nematic susceptibility, proportional to $1/a_n$, does not diverge. We emphasize that the actual renormalized nematic susceptibility does diverge, due to the contribution from the lattice degrees of freedom. The behavior of $\frac{\partial\psi}{\partial\varepsilon_3}$ in the disordered state is similar to the experimentally observed behavior of $m_{12} - m_{11}$ for the undoped composition $\mathrm{BaNi_2As_2}$.

In contrast, in the region of the phase diagram where the transition is electronically-driven, $\frac{\partial\psi}{\partial\varepsilon_3}$ displays a clear peak at the transition temperature $T_{\mathcal{N}}$ and, within mean-field, a Curier-Weiss temperature dependence. This behavior is reminiscent of that of $m_{12} - m_{11}$, in the disordered phase, for underdoped and near optimally-doped $\mathrm{Ba_{1-x}Sr_xNi_2As_2}$.

II. SUPPORTING EXPERIMENTAL DATA

A. X-Ray Diffraction and Charge Order

Figure S3 displays $(H\ K)$ mappings of reciprocal space, illustrating a representative I-CDW x-ray scattering peak in $\mathrm{Ba_{1-x}Sr_xNi_2As_2}$ single crystals. I-CDW superstructure reflections are observed only in the tetragonal phase, at temperatures near the tetragonal-triclinic structural transition. The I-CDW abruptly vanishes upon transitioning to the low temperature triclinic structure, within which a new, commensurate superstructure is observed. Appearing with a $(0.28\ 0\ 0)$ periodicity in $\mathrm{BaNi_2As_2}$, the superstructure wave vector appears to have a slight substitution dependence, appearing closer to $(0.27\ 0\ 0)$ in samples of $x = 0.4$. Additionally, broader superstructure reflections are observed in $x = 0.4$ samples than those in $x = 0$. Estimates derived from peak full width at half maximum values suggest a correlation length of approximately 330 Å at $x = 0.4$. I-CDW peak widths in $x = 0$ samples, meanwhile, are narrower than the resolution of the experimental apparatus, placing a lower bound on the correlation length of nearly 1000 Å. In both $x = 0$ and $x = 0.4$ crystals superstructure reflections are unidirectional, observed only along $(H\ 0\ 0)$ and not in the orthogonal $(0\ K\ 0)$ direction, breaking B_{1g} symmetry. Despite this symmetry breaking, no concurrent orthorhombic distortion is observed at the I-CDW onset within the resolution of the instrument. In more heavily substituted samples of $\mathrm{Ba_{0.35}Sr_{0.65}Ni_2As_2}$ ($T_S = 60$ K) the incommensurate peaks are not visible at 65 K (or any other measured temperature). While only a single representative peak is displayed in Fig. S3, I-CDW reflections have been observed across several Brillioun zones in $\mathrm{BaNi_2As_2}$ and $\mathrm{Ba_{0.6}Sr_{0.4}Ni_2As_2}$, and are absent in the entirety of visible k-space at all temperatures in $\mathrm{Ba_{0.35}Sr_{0.65}Ni_2As_2}$ and $\mathrm{Ba_{0.28}Sr_{0.72}Ni_2As_2}$. All samples with an observable structural distortion ($x < x_c$) exhibit C-CDW peaks in the triclinic phase which are not displayed here.

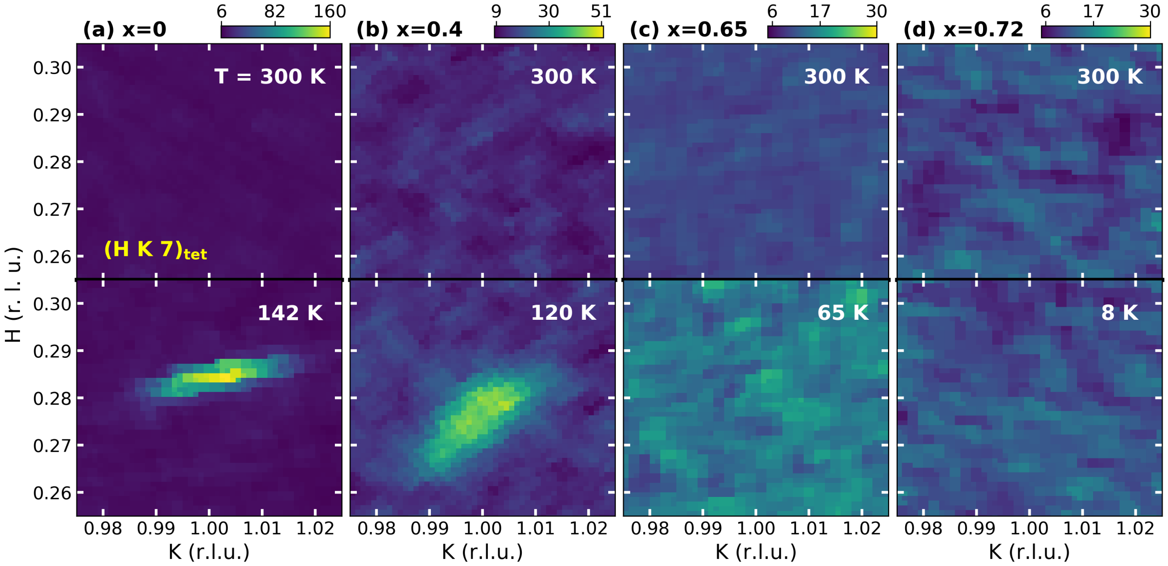

FIG. S3. **I-CDW x-ray reflections in $Ba_{1-x}Sr_xNi_2As_2$ single crystals**. (H K) k-space mapping of x-ray scattering intensity in $Ba_{1-x}Sr_xNi_2As_2$ single crystals in the neighborhood of (H K L) coordinates (0.28 1 7). Data are presented at $x = 0$ (a), 0.4 (b), 0.65 (c), and 0.72 (d). Top panel displays k-space mapping at 300 K, where no superstructure reflections are visible for all x. The lower panel displays data collected at temperatures just above the tetragonal-triclinic structural transition temperature for $x = 0$, 0.4, and 0.65. Specimens of $x = 0.72$ exhibit no structural transition, however, thus the lower panel of (d) instead displays the k-space intensity map collected at the base temperature of the experiment, 8 K.

B. Crystal Properties

Chemical and structural characterization of single crystals grown across the $Ba_{1-x}Sr_xNi_2As_2$ substitution series were performed to create the phase diagram presented in the main text and to confirm crystal qualities. The results of these studies are presented in Fig. S4.

For the structural refinement with the x-ray diffraction data, we measured 1800+ single crystal reflections of which 165+ were unique. Given that it is a tetragonal crystal system, only two lattice parameters were refined, a and c. All atoms sit on a special position except for As, which is on the (1/2 1/2 z) site. Therefore only one fractional coordinate was refined. For the Sr/Ba alloyed site, the occupancies of both were refined with the total occupancy constrained to unity. Anisotropic atomic displacement parameters (ADPs) were refined for each atom. Again, the tetragonal symmetry imposes constraints on the number of unique parameters and six independent ADPs were therefore refined.

EDS experiments performed on $Ba_{1-x}Sr_xNi_2As_2$ specimens indicate that near $x = 0.5$ a discrepancy emerges between the nominal Sr content used in the growth, and the actual x value observed in single crystals [Fig. S4(b)]. When actual concentrations differ from nominal, careful characterization is required to ensure knowledge of the actual x value. In this study, both EDS and single-crystal x-ray diffraction measurements were performed to determine x. A direct comparison of EDS values (x_{EDS}) with those determined from Rietveld refinement values of single crystal x-ray diffraction data (x_{x-ray}) is provided in Fig. S4(c), confirming very good agreement. Additionally, refinement analysis yields very low R_1 error values as shown in Fig. S4(g) indicating good crystallinity for samples across the entirety of the phase diagram.

Additionally, structural parameters of $Ba_{1-x}Sr_xNi_2As_2$ single crystals collected from single crystal x-ray diffraction experiments at 250 K exhibit a subtle feature in the a-axis lattice parameter and tetrahedral bond angles near $x_c = 0.7$ [Fig. S4(d-f)]. These features coincide with a sudden quench of the structural distortion, implying a change in interatomic bonding near x_c may render the system inhospitable to the triclinic phase. Analogy to the iron based systems suggests this change may take the form of an interaction between interlayer arsenic atoms. Such an effect (as is observed in $CaFe_2As_2$ under pressure [2, 3]) breaks no crystal symmetries and occurs as the interlayer As-As separation approaches 3 Å, both of which are consistent with observations here. However, in the iron-based compounds interlayer As atoms will form a strong bond causing a dramatic collapse in the crystallographic c-axis, an abrupt reduction in As-As spacing, and an expansion of the transition metal-pnictogen layer, all of which are absent in the $Ba_{1-x}Sr_xNi_2As_2$ series. Thus, if an interaction between interlayer arsenic atoms is responsible for the structural

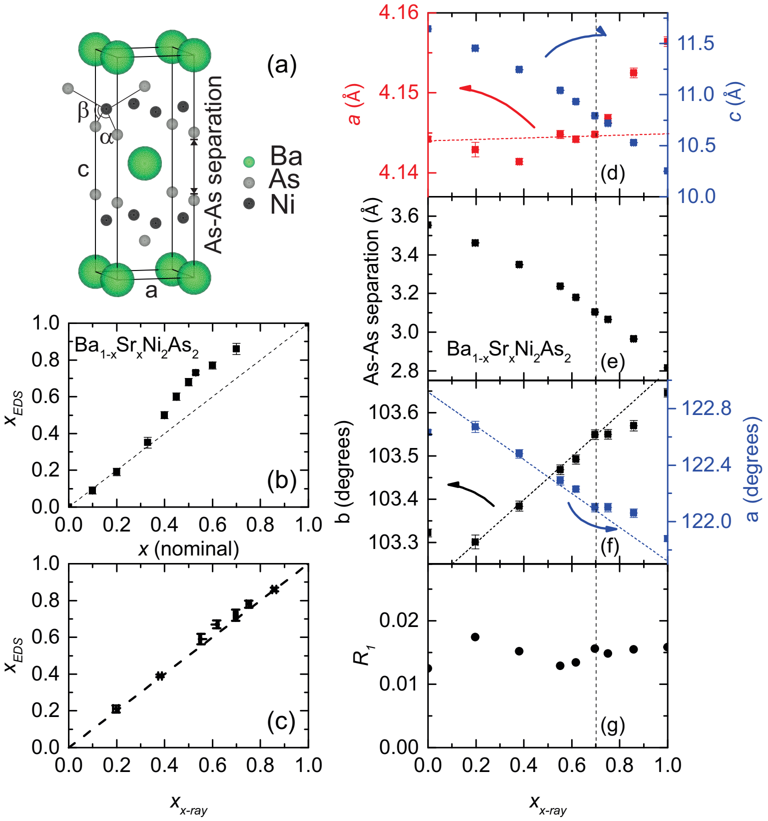

FIG. S4. **Structural and chemical properties of $\mathbf{Ba_{1-x}Sr_xNi_2As_2}$ single crystals.** (a) Crystal structure of tetragonal $BaNi_2As_2$. (b) Evolution of actual Sr content (determined via EDS) versus nominal value included in the growth. (c) Comparison of x values determined via EDS and x-ray diffraction experiments. (d-g) x dependence of a and c lattice parameters (d), As-As spacing (e), and tetrahedral bond angles (f) in $Ba_{1-x}Sr_xNi_2As_2$ single crystals, and R_1 error values. All data are collected at 250 K. The dashed line running vertically through panels (d-g) denotes critical concentration, x_c, where the system undergoes a zero temperature structural phase transition. Error bars represent standard error determined by least squared refinement.

anomaly in $Ba_{1-x}Sr_xNi_2As_2$ samples, it manifests in a fundamentally different manner than has been reported for iron-based compounds.

C. Resistivity, Magnetism and Specific Heat

Figure S5 displays basic magnetic and transport properties of $Ba_{1-x}Sr_xNi_2As_2$ single crystals. Temperature hysteretic anomalies indicate the onset of the first order tetragonal-triclinic structural distortion. The location of these anomalies was used to construct the phase diagram presented within the main text. Magnetization data similarly track the structural distortion, producing a sharp downward anomaly at the phase transition.

The low temperature resistive and ac-magnetic signatures of superconductivity are presented in Fig. S5(b,d). While $Ba_{1-x}Sr_xNi_2As_2$ crystals in the range of $0.4 < x < 0.7$ exhibit transport and magnetic signatures of superconductivity at temperatures as high as 2.5 K, these signatures are significantly broadened in temperature compared to samples outside of this range. Furthermore, no heat capacity jump is observed at the magnetic and resistive superconducting transitions in these samples. Apparent superconducting signatures in transport and magnetic measurements are therefore believed to originate from superconducting filaments rather than a bulk superconducting phase, with bulk T_c remaining effectively constant for all crystals in the low temperature triclinic structure.

That T_c enhancement in undersubstituted samples is filamentary in nature is observed clearly in resistivity, heat capacity, and magnetization measurements collected from a single representative underdoped $x = 0.68$ crystal [Fig. S6(a-d)]. Heat capacity and transport measurements confirm a hysteretic tetragonal to triclinic structural transition [Fig. S6(a)]. Data taken below 5 K exhibit resistive and magnetic superconducting signatures that are broadened,

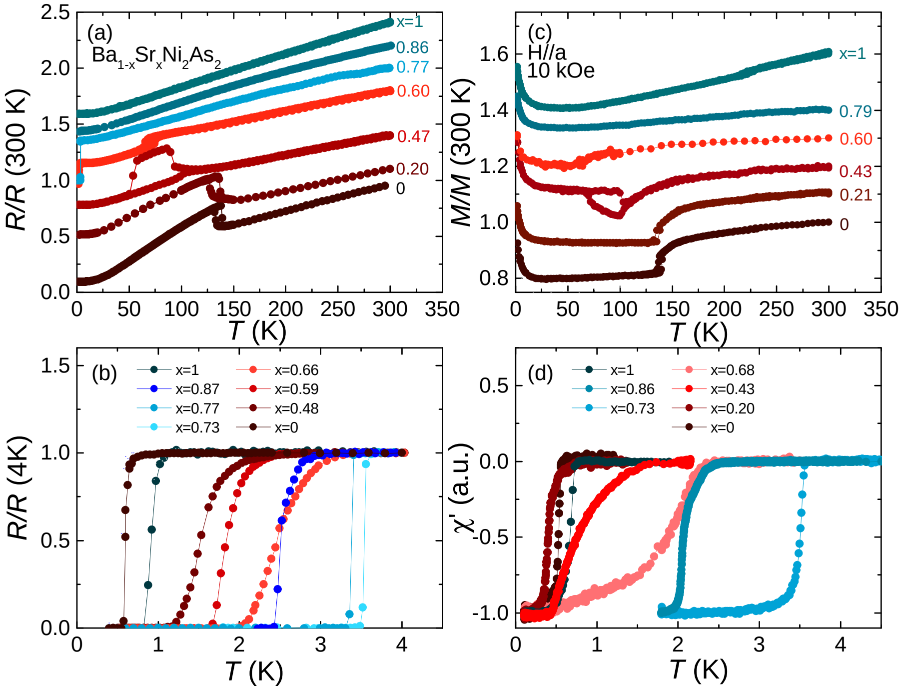

FIG. S5. **Physical properties of $Ba_{1-x}Sr_xNi_2As_2$ single crystals.** Temperature dependent normalized resistivity data are presented for $Ba_{1-x}Sr_xNi_2As_2$ single crystals at high (a) and low (b) temperatures. Temperature hysteretic anomalies in (a) coincide with the tetragonal-triclinic distortion. (c) DC magnetization data collected at 10 kOe with $H \parallel a$ are presented. Sharp, temperature hysteretic anomalies at high temperature indicate structural transition, while divergence at low temperature likely originates from paramagnetic impurities. (d) Low temperature ac-magnetic susceptibility showing superconducting transitions. In all panels samples plotted in red (blue) are triclinic (tetragonal) at lowest temperatures.

and occur at approximately 2 K. Heat capacity data, however, shows a sharp anomaly at a much lower temperature, 0.5 K [Fig. S6(d)]. This behavior has been observed across a number of samples, and no crystals have been found where both the triclinic structural distortion and a bulk enhancement of superconducting T_c compared with the $BaNi_2As_2$ end-member (determined by heat capacity experiments) are present.

Heat capacity measurements in $Ba_{1-x}Sr_xNi_2As_2$ crystals show a clear discontinuity in Debye temperature when crossing the zero temperature structural phase boundary [Fig. S7(c)]. In the oversubstituted samples, the Debye temperature remains effectively constant between $x = 0.7$ and $x = 0.87$ before increasing in the $SrNi_2As_2$ end member. The Sommerfeld coefficient (γ) exhibits a minimal x dependence across the phase diagram, decreasing modestly between $x = 0$ and $x = 1$. Both Debye temperature and Sommerfeld coefficient are extracted from heat capacity data using an Einstein-Debye model.

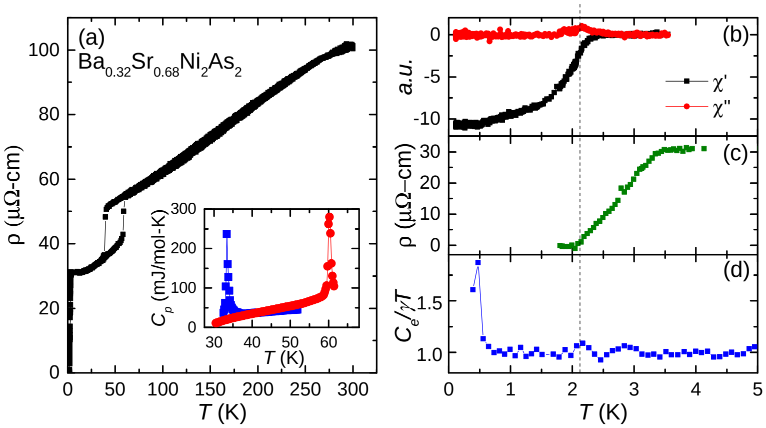

FIG. S6. **Physical properties of a single $Ba_{1-x}Sr_xNi_2As_2$ crystal of $x = 0.68$.** (a) Transport data are taken between 1.8 and 300 K in a $Ba_{1-x}Sr_xNi_2As_2$ sample of $x = 0.68$. Inset displays heat capacity data collected over the tetragonal-triclinic structural transition in the same crystal specimen. Anomalies associated with the structural transition are observed in heat capacity, showing it is of bulk origin and is strongly first order. (b-d) Magnetization (b), transport (c), and heat capacity (d) superconducting transitions observed again in the same single crystal measured in panel (a). While magnetization and transport signatures suggest a T_c of approximately 2 K, a heat capacity anomaly is only observed near 0.5 K, indicating the bulk superconducting T_c is virtually identical to the $BaNi_2As_2$ end-member.

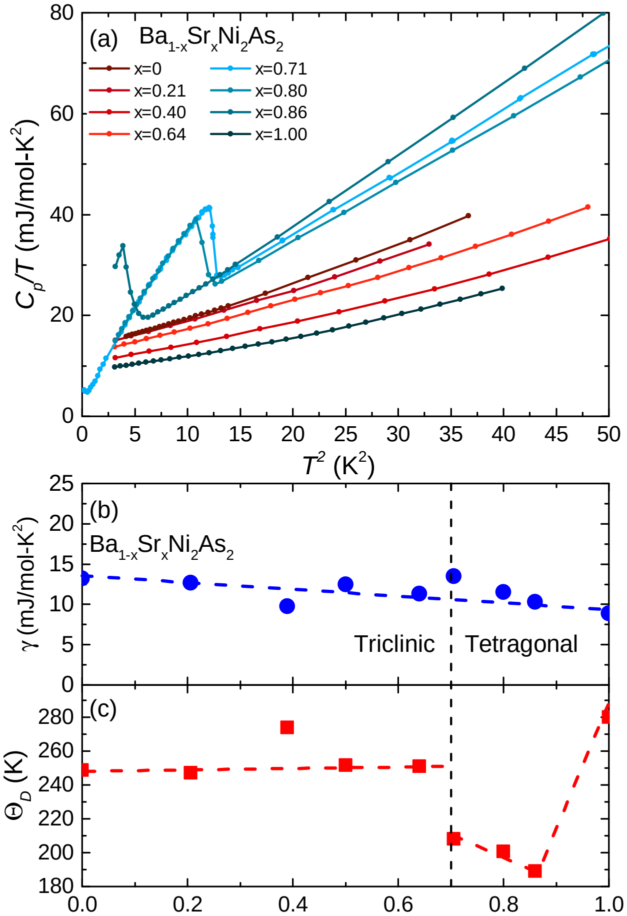

FIG. S7. **Heat capacity data for $Ba_{1-x}Sr_xNi_2As_2$ series.** (a) C_p/T vs T^2 values are presented for many x in the $Ba_{1-x}Sr_xNi_2As_2$series. Data denoted with red (blue) symbols indicate that samples of this concentration favor a triclinic (tetragonal) structure at lowest temperature. Evolution of the Sommerfeld coefficient (b) and Debye temperature (c) are included as a function of x. Dashed line running vertically through $x_c = 0.7$ denotes the critical Sr concentration when the system transitions from triclinic to tetragonal crystal symmetries at lowest temperature.

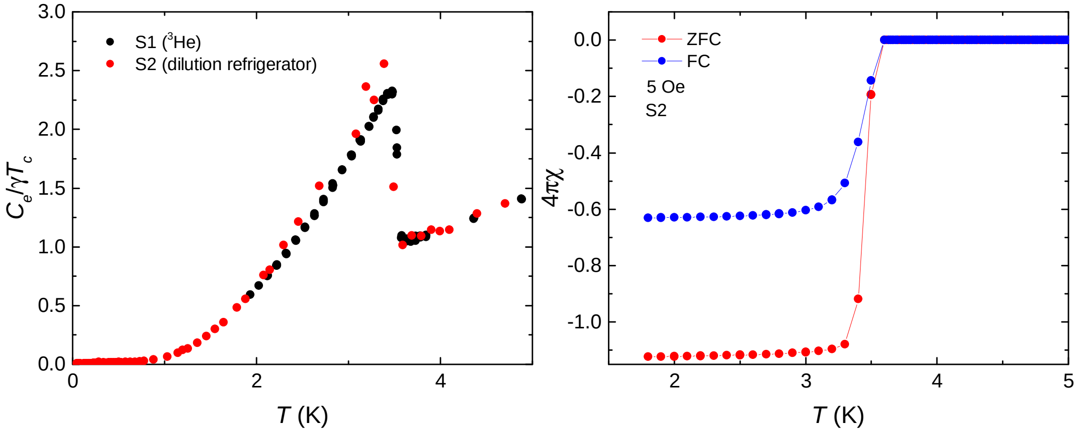

FIG. S8. **Heat capacity of optimally substituted Ba$_{1-x}$Sr$_x$Ni$_2$As$_2$ crystals**. (a) Heat capacity data for two Ba$_{1-x}$Sr$_x$Ni$_2$As$_2$ crysals with $x = 0.71$ samples measured using measured using a 3He PPMS system (S1) and a dilution refrigerator system optimized for low temperature measurements (S2). (b) Magnetic susceptibility of sample S2.

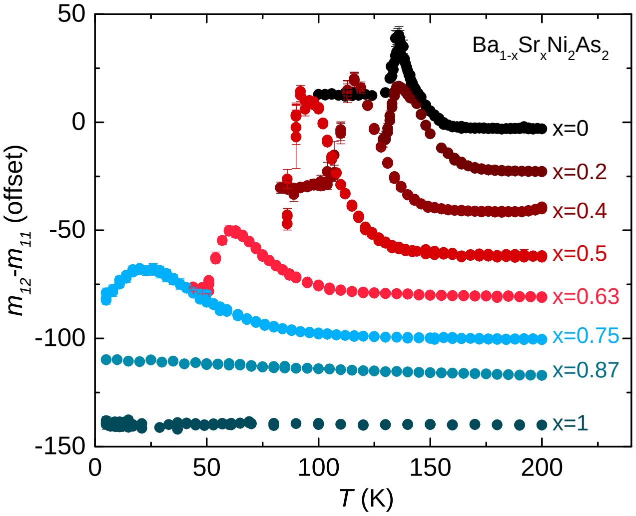

FIG. S9. **$m_{12} - m_{11}$ elastoresistivity of Ba$_{1-x}$Sr$_x$Ni$_2$As$_2$ single crystals**. B_{1g} symmetric elastoresistivity for Ba$_{1-x}$Sr$_x$Ni$_2$As$_2$ single crystals of select x are presented. Data denoted with red (blue) symbols indicate that samples of this concentration favor a triclinic (tetragonal) structure at lowest temperature. Values presented here were used to generate the contour plot presented in the main text. Error bars represent the 90% confidence interval of linear fitting.

D. Optimal Substitution

The sharp superconducting transition in optimally substituted Ba$_{1-x}$Sr$_x$Ni$_2$As$_2$ crystals was observed to be robust, appearing as sharp anomalies in all measured samples. Figure S8a presents the results of low temperature heat capacity experiments for two different samples measured in two separate experimental apparatus. The data for sample S1 is provided in Fig. 2 in the main text. The vanishing heat capacity and full volume fraction superconductivity [Fig. S8b] observed in the zero temperature limit of sample S2 indicates that the entire sample enters the superconducting phase.

E. Elastoresistivity

Figure S9 displays the measured elastoresistivity for Ba$_{1-x}$Sr$_x$Ni$_2$As$_2$ single crystals of select x. Data are staggered by a constant offset. Figure S10 displays the measured elastoresistivity for both BaNi$_2$As$_2$ and BaFe$_2$As$_2$ single crystals. BaNi$_2$As$_2$ B_{2g} symmetric elastoresistivity exhibits almost no response to the onset of nematic order. The B_{1g}

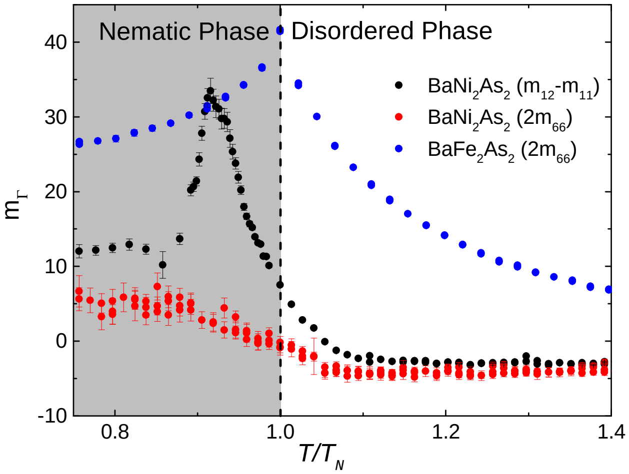

FIG. S10. **Elastoresistivity comparison, $BaNi_2As_2$ and $BaFe_2As_2$.** Elastoresistivity is plotted versus normalized temperature (normalized to the nematic transition temperature, $T_{\mathcal{N}}$) for $BaNi_2As_2$ and $BaFe_2As_2$ single crystals. Data are provided below $T_{\mathcal{N}}$, though, due to the structural change and, in the case of $BaNi_2As_2$, onset of elastoresistive hysteresis, these data are no longer well defined symmetry isolated elastoresistive components. Error bars represent 90% confidence interval of linear fitting.

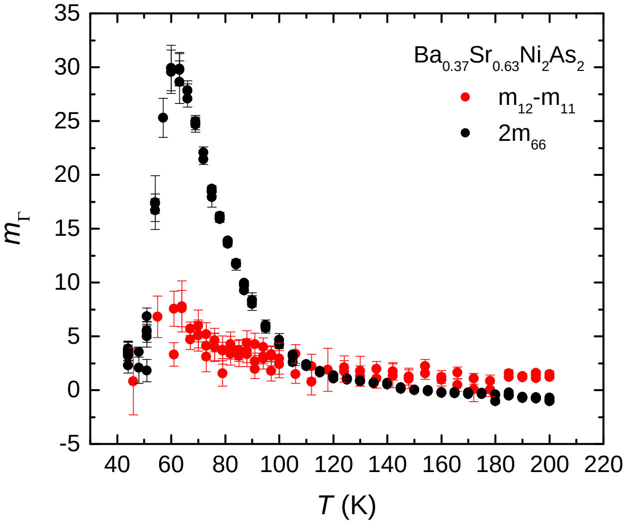

FIG. S11. **Elastoresistivity in undersubstituted $Ba_{1-x}Sr_xNi_2As_2$.** B_{1g} and B_{2g} symmetric nematic susceptibility for samples of $x = 0.63$. Data exhibits a Curie-Weiss reminiscent temperature divergence in the B_{1g} channel, while B_{2g} symmetric susceptibility does not diverge. Error bars represent 90% confidence interval of linear fitting.

symmetric elastoresistivity $(m_{12} - m_{11})$ similarly does not diverge approaching the nematic transition in unsubstituted $BaNi_2As_2$, a fact made more obvious through comparison to the clear divergence seen in $BaFe_2As_2$. Meanwhile, in samples of $x = 0.63$, a clear divergence in B_{1g} symmetric elastoresistivity is observed approaching the structural transition, reminiscent of the B_{2g} response in $BaFe_2As_2$ (Fig. S11). The m_{66} elastoresistivity coefficient in $x = 0.63$ shows virtually no temperature dependence, however, indicating that B_{2g} symmetric nematic fluctuations do not strengthen significantly in the $Ba_{1-x}Sr_xNi_2As_2$ series with increasing x.

$Ba_{1-x}Sr_xNi_2As_2$ specimens of $x = 0.75$ show a large $m_{12} - m_{11}$ elastoresistive response, reaching a maximum value of nearly 35. X-ray diffraction measurements show no structural distortion or superstructure reflections between room temperature and 8 K, while transport measurements do not indicate of a phase transition [Fig. S12(a,b)]. Despite the absence of any apparent transition $m_{12} - m_{11}$ coefficients display a clear peak and subsequent downturn near 25 K [Fig. S12(c)].

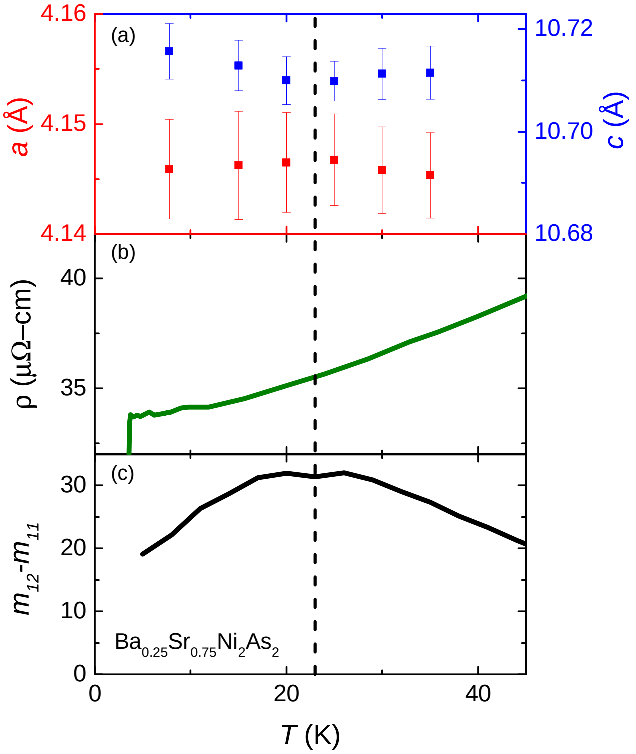

FIG. S12. **Physical properties of optimally substituted $\mathbf{Ba_{1-x}Sr_xNi_2As_2}$.** (a-c) Evolution of *a* and *c* crystallographic lattice parameters (a), resistivity (b), and elastoresistivity (c) as a function of temperature in optimally substituted $Ba_{1-x}Sr_xNi_2As_2$. While elastoresistivity displays a peak, no sign of an apparent phase transition is observed in either transport or structural measurements. Error bars represent standard error determined through least square fitting.

---

[1] Cowley, R. A. Acoustic phonon instabilities and structural phase transitions. *Phys. Rev. B* **13**, 4877-4885 (1976).

[2] Kreyssig, A. *et al.* Pressure-induced volume-collapsed tetragonal phase of $CaFe_2As_2$ as seen via neutron scattering. *Phys. Rev. B* **78**, 184517 (2008).

[3] Saha, S. R. *et al.* Structural collapse and superconductivity in rare-earth-doped $CaFe_2As_2$. *Phys. Rev. B* **85**, 024525 (2012).